CrossMark

Fracture Toughness of Thermal Spray Ceramics: Measurement Techniques and Processing Dependence

Gregory M. Smith[1] · Adam Smith[1] · Sanjay Sampath[1]

Abstract Fracture toughness measurements are critical for materials design and characterization but can be difficult to perform on overlay coatings due to a range of geometric factors and substrate constraints. Thermal spray (TS) coatings bring additional complications to measurement interpretation due to their defected, anisotropic structures. Toughness of free-standing coatings has been studied in the past, and literature results indicate promise in measurement with a range of methods. One of these, single-edge, notched beam (SENB) method offers a straight forward approach for measuring fracture toughness and lends itself well for use with TS coatings. In this work, SENB method is used with deliberate modifications to specific parameters of the test specimens, namely free-standing thickness, notch depth, notch sharpness, and heat treatment state, to ascertain the impact of these modifications on the measurement results for air plasma spray Al_2O_3. Additionally, two methods adapted from the literature, a modified adhesion method and a tensile elongation method, are evaluated for use with three different Al_2O_3 coatings, including by air plasma spray, flame spray, and high velocity oxy-fuel processes. Results indicate good correlation between SENB and the modified methods for all three coating variants and give insight into the orientation-dependent toughness properties of TS coatings.

Keywords cracking · fracture · mechanical properties · microstructure · tensile bond strength

✉ Gregory M. Smith
  gregory.m.smith@stonybrook.edu

[1] Center for Thermal Spray Research, Stony Brook University, Stony Brook, NY 11794, USA

Introduction

Ceramics, glasses, and ceramic composite materials have been used across various industries and have seen numerous advances with regard to materials versatility, processing, and applications for structural and functional uses (Ref 1). Ceramic materials are notable for their potential high stiffness and strength, but also their lack of plasticity and propensity for brittle failure linked to internal flaws (Ref 2, 3). This can be overcome to some extent through creative material design. There are a range of bio-materials and ceramic composites which use advantageous engineering, orientation/layering, and hierarchical structures to achieve increased damage tolerance (Ref 4, 5). Damage tolerance in this context can be described as the ability to limit or arrest crack propagation despite the presence of internal defects or flaws within the system, often originating from the material's formation or processing. These defects can manifest as internal crack origination sites or as internal stress concentration points.

Measurement of a crack and characterization of its propagation can be inherently difficult. A variety of techniques have been developed for measurement of crack growth resistance and fracture toughness, but often are narrow in scope and limited to a specific material or material class. Different methods focus on distinct orientations, geometric factors, and size constraints, and as such there is no "one size fits all" test. This can introduce challenges when more broadly comparing material measurements. For this reason, measurement methodology is critical. For example, indentation methods for measuring fracture toughness are sometimes applicable for use with dense glassy materials. However, there is a strong consensus in the literature that these measurement methods are inadequate for many other materials, including porous

materials and those containing high levels of internal cracking and defects, such as thermal spray coatings (Ref 6).

Generally, the governing equations for fracture toughness methods assume linear-elastic, isotropic material behavior. In bulk materials, crack propagation is more likely to occur at intra-granular sites or along grain boundaries, depending on the material's intrinsic qualities and loading conditions. TS coatings have additional structural implications due to splat-based material buildup, which can act as new initiation sites and pathways for crack propagation. This multitude of potential initiation sites can have implications on the toughness measurement. Additionally, the rapid solidification and quenching splats experience during deposition can result in fine grain structures and tensile residual stresses, the latter which can augment the driving force for crack growth.

The high level of anisotropy found in TS materials also implies a strong dependency on orientation when measuring material properties. Quantifying sample orientation, mode of failure, and crack propagation direction is critical. For example, delamination failure in TBCs typically occurs within the coating, above the thermally grown oxide (TGO) layer, parallel to the interface and the underlying substrate (Ref 7). For that application, in-plane orientated toughness (where crack propagation is parallel to the substrate) is the critical property to measure. Out-of-plane toughness, measured with crack propagation orthogonal to the substrate would not directly relate to the understood failure mechanism in that TBC system. This orientation dependence has been evaluated to some degree in the recent literature, for example by Choi et al. (Ref 8) who looked at mode mixity and the implications of different fracture and failure modes of crack propagation in APS coatings and by Smith et al. (Ref 9) who performed direct measurement of toughness dependent on anisotropy in thick YSZ coatings. Both offer unique assessment of orientation and anisotropic behavior, but do not represent a full field assessment a wide range of TS structures. Other single orientation toughness measurements have been performed on TS coatings in the literature, but their complexity can limit wide-scale usage (Ref 9-12). In fracture toughness testing of TS materials, one of the largest challenges is sample fabrication. Standardized fracture toughness methodologies often call for specimen geometries that differ from what is approachable with typical TS deposition techniques. TS coatings generally have a thickness ceiling of $\sim$ 2 mm. This is sufficient for out-of-plane testing; however, this thickness limitation makes in-plane toughness measurement difficult. Even after fabricating a coating of sufficient thickness, delaminating the coating from the substrate (either by dissolution of the substrates or through mechanical means) has the potential to alter the material's physical structure.

Bend testing offers relative ease of sample fabrication, test preparation, and interpretation of the results. Both three- and four-point variants can be used with a range of pre-crack notch geometries, including single-edge notched beam (SENB) and chevron notch geometries. These methods have been successfully used in the past with TS materials (Ref 8, 9, 13, 14). The notch and pre-crack geometries induce a localized stress concentration during mechanical loading resulting in crack propagation. The critical load at which failure occurs combined with the known specimen dimensions can be used to calculate fracture toughness. Several ASTM standards describe this relation for a number of notch geometries (Ref 15, 16).

In the work presented here, multiple methods are evaluated to compare the fracture toughness measurement of different TS Al_2O_3 materials. This includes the benchmarking of standard SENB and chevron notch testing with a set of standard reference materials (bulk Al_2O_3, quartz glass, and sintered SiC), and an expanded parametric study of a single sprayed material system with intentionally introduced sample variation This entailed changes to thickness, notch depth, and notch sharpness. Two additional test methodologies (modified tensile adhesion and tensile elongation) are proposed here, extracted from non-TS literature. These methods have been adapted here to measure orientation specific fracture toughness on three different Al_2O_3 TS microstructures that can broadly represent a range of TS ceramic structures. TS Al_2O_3 represents a low-cost material that is readily sprayable over a range of thickness, with easily tailorable structures and properties. This presents a platform for evaluation of these techniques to quantify orientation-dependent failure in ceramics TS coatings.

Experimental

Coating Fabrication

Three different coating processes were used to encompass a wide design space of ceramic TS structures and corresponding properties. These included standard air plasma spray (APS), high velocity oxy-fuel (HVOF), and rod-fed flame spray processes. Specific deposition was performed using Al_2O_3 feedstocks tailored to each spray process. Table 1 shows the materials and processes used to produce the three coatings. Coatings were deposited on AISI low-carbon steel plates (228 mm $\times$ 25.4 mm $\times$ 2.4 mm), steel tensile bars (152 mm $\times$ 25.4 mm $\times$ 3.2 mm, with 65 mm $\times$ 12.7 mm gauge), and 25.4 mm diameter steel adhesion slugs. Substrates were grit-blasted at 5.5 bar with Al_2O_3

Table 1 Process parameters for three different coating variations

| Deposition torch/process designation	Feedstock	Relevant process parameters
Rod flame spray (Rokide, Saint Gobain, Worcester, MA)	6 mm Al_2O_3 rod (St. Gobain, Worcester, MA)	40 SLPM C_2H_2, 40 SLPM O_2, 150 mm spray distance, 250 mm/min rod feed rate
APS (3 MB, Oerlikon Metco, Westbury, NY)	105 NS (Oerlikon Metco, Westbury, NY)	550 Amps, 40 Ar, 6 H_2, 100 mm spray distance, 35 g/min feed rate
HVOF (HV-2000, Thermach, Appleton, WI)	Al-1110-HP (Praxair, Indianapolis, IN)	1500 SCFH H_2, 600 SCFH O_2, 152 mm spray distance, 7.5 g/min feed rate

grit. Air cooling was used to control fixture temperatures and samples underwent preheating prior to deposition.

Three-Point Bend Testing and Notch Geometries: SENB and Chevron

Free-standing coating specimens are required for bend testing. To intentionally delaminate the coating from the substrate, careful cantilever bending was used. Edges of the coated beams were polished to remove overspray. A small strip of coating was removed from the end of the substrate, exposing of the underlying metal. This end was held in a vice and the higher stiffness coating easily delaminated after simply flexion. Once delaminated, 25.4 mm × 6 mm strips were cut using a high-speed diamond coated metallographic saw and mechanically ground to a 9-μm surface finish. After delamination, half of the SENB samples were sintered for 24 h at 1200 °C.

Following sample sectioning and heat treatment, two different notch geometries were evaluated; a standard single-edge notch and a chevron notch. These are governed by ASTM E 1820 and ASTM C 1421, respectively (Ref 15, 16). Both methods evaluate fracture toughness based on the principle that loading energy is concentrated over a small area, which serves as the eventual crack initiation site. For the SENB methodology, this initiation site spans the width of the sample beneath the notch, while the chevron testing concentrates the loading energy to the sharp convergence point at the tip of the chevron. In the chevron configuration, the crack propagates from the chevron tip through the increasing material width which promotes more stable crack behavior. The measured initiation fracture toughness is a function of the sample geometry and measured load at which failure occurs. Figure 1 shows a schematic summarizing the notching and testing of the SENB samples.

Samples were notched using a diamond saw attached to a rotary tool, which was rastered across the sample surface at approximately 1 Hz, increasing depth slightly after each pass. The samples were held flat for the standard single-
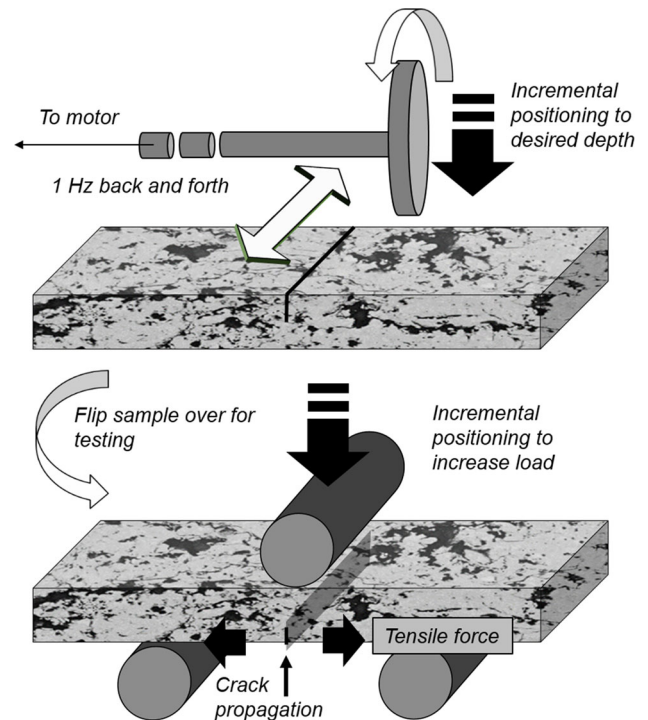
Fig. 1 Notching of SENB specimens and three-point bend test setup

edge notch (with resulting notch shown in Fig. 2a) and held at an angle to cut away each side of the eventual chevron notch. The chevron sample is rotated so that its base lies at an angle to the platform (between 30° and 45° depending on sample dimensions). Material is removed in two cuts, with resulting chevron remaining, shown in Fig. 2(c). Extra sharpening of the SENB notch was also performed on one set of the samples to determine the effects of notch sharpness, shown in Fig. 2(b). The notch was enhanced using a sharp razor blade and 0.5 μm diamond lapping paste (McMaster-Carr).

A parametric study was performed on the APS Al_2O_3 coating with a total of 24 different variations evaluated using the SENB technique (parametric variations listed in Table 2). The parametric evaluation was focused on two primary thickness differences. Additional, extra-thin 1.01 mm samples were included as test points for a

separate thickness comparison at the standard notch depth/ sharpness, in their as-sprayed conditions. The standard/center condition values for the 1.63 mm thickness were used for comparison with the results of the modified tensile adhesion and tensile elongation methods. Comparison of the chevron and SENB results was performed with

stress concentration to the notch geometry. In the $Y_{\min}^*$ term, a_0 and a_1 represent the distance from the chevron tip to sample base, and chevron base to sample base, respectively (Ref 15, 16).

$$K_{\mathrm{Ic}} = \frac{P_c L}{BW^{3/2}} \cdot F\left(a/W\right) \qquad (\text{Eq 3})$$

$$F\left(a/w\right) = \frac{3\left(a/W\right)^{1/2}\left[1.99 - \left(a/W\right)\left(1 - a/W\right)\left(2.15 - 3.93\left(a/W\right) + 2.7\left(a/W\right)^2\right]\right.}{2\left(1 + \frac{2a}{W}\right)\left(1 - a/W\right)^{3/2}} \qquad (\text{Eq 4})$$

like-dimensioned, 3.25 mm thickness samples due to limitations arising from the difficulty in fabricating chevron notches in thinner samples.

$$K_{\mathrm{Ivb}} = Y_{\min}^* \left[\frac{P_c L}{BW^{3/2}}\right] \qquad (\text{Eq 5})$$

$$Y_{\min}^* = \frac{0.7601 - 3.634\left(a_0/W\right) + 3.1165\left(a_1/W\right) - 1.2782\left(a_1/W\right)^2 + 0.3609\left(a_1/W\right)^3}{1.000 - 3.119\left(a_0/W\right) + 3.0558\left(a_0/W\right)^2 - 1.0390\left(a_0/W\right)^3 + 0.0608\left(a_1/W\right)} \qquad (\text{Eq 6})$$

Governing Equations and Operational Description

Loading was performed on a universal testing machine (Model 26005, TIRA GmbH, Germany) configured for three-point loading, with 21 mm span between the posts. Loading occurred at 0.06 mm/min crosshead speed and was monitored by additional laser displacement (LM100-ANR12501, Panasonic SUNX, Japan) and a 200-N load cell. From this test setup, both flexural strength (using an unnotched specimen) and toughness testing was performed. Flexural strength and flexural modulus can be measured simply from the unnotched beam and calculated from Eq 1 and 2. In the following equations, P_c is the maximum applied load, L is the loading span (constant at 21.06 mm) of the bend test setup, B is the sample width, W is the sample thickness, and d is the deflection of the beam at the maximum applied load.

$$\sigma_{\mathrm{flex}} = \frac{3P_c L}{2BW^2} \qquad (\text{Eq 1})$$

$$E_{\mathrm{bend}} = \frac{L^3 P_c}{4BW^3 d} \qquad (\text{Eq 2})$$

Fracture toughness measurement by SENB (Eq 3 and 4) and chevron (Eq 5 and 6) technique can be calculated according to the equations below, where notch depth, a, is incorporated into the calculations. Equation 3 and 5 contain geometric factors $F\left(a/w\right)$ and $Y_{\min}^*$, which relate the

Alternative Methods for Determination of Fracture Toughness

In the previously described loading scenarios, the three-point bend testing achieves only out-of-plane measurement of coating toughness. This is not universally applicable to TS coating failure because many fail via in-plane mechanisms (e.g., TGO-induced failures in TBCs). Measurement of such failure can be difficult with SENB geometries when sample thickness is limited. Here, two additional methods are proposed to evaluate orientation-dependent toughness, namely a modified tensile adhesion technique (enabling in-plane toughness measurement) and a tensile elongation technique (enabling out-of-plane toughness measurement). Schematics of both proposed tests are shown in Fig. 3.

Modified Tensile Adhesion Method

Standard adhesion strength of thermal spray coatings is commonly measured by ASTM C633, which acts as the de facto industrial standard (Ref 17). This technique has notable shortcomings for adhesion strength measurements; however, the basic loading scenarios are applied here to extrapolate fracture toughness (Ref 18). Modification of this technique to measure interfacial failure and in-plane
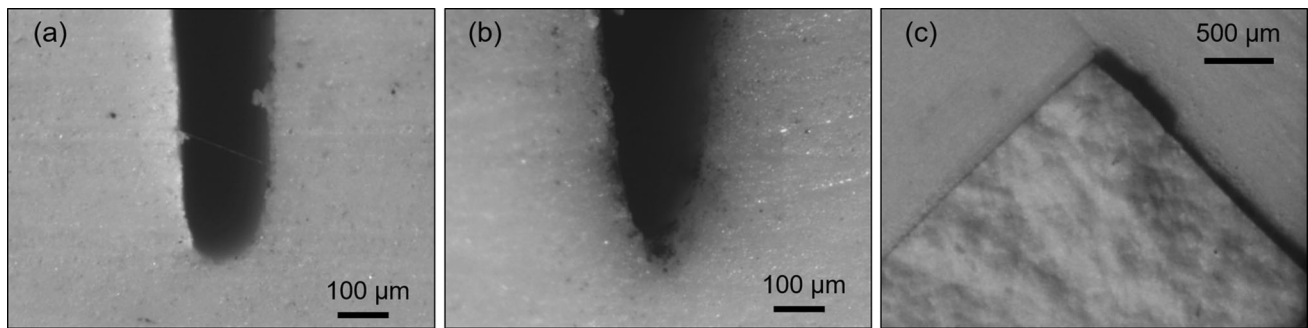
Fig. 2 Light micrographs of (a) standard, (b) enhanced, and (c) chevron notch geometries. Crack propagation begins from the bottom of the notch in (a) and (b), and at the tip of the chevron in (c), and travels toward to bottom of the images

Table 2 Sample and notch variation changes for APS Al$_2$O$_3$ parametric study

Sample thickness (W)	Notch depth ratio (a/W)	Notch sharpness	Sample condition
3.25 ± 0.09 mm	0.35 ± 0.02	Standard, 80 μm root radius	As-sprayed
1.63 ± 0.09 mm	0.48 ± 0.03	Razor Enhanced, 45 μm root radius	Sintered
…	0.66 ± 0.01	…	…

Fig. 3 Setup and testing approaches to the modified tensile adhesion method (a) for measuring in-plane fracture toughness and the tensile elongation method (b) for measuring out-of-plane fracture toughness
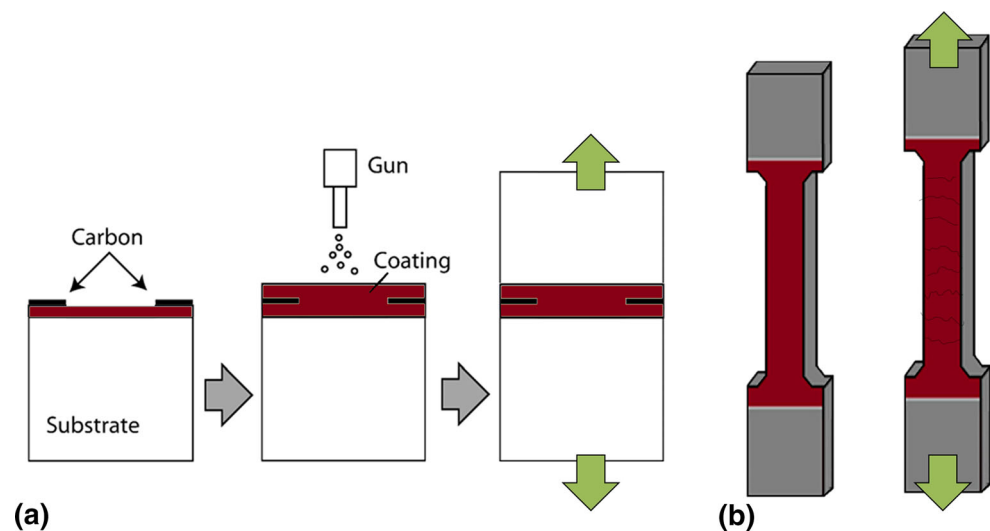
fracture toughness by use of a modified interfacial surface has been performed in the past (Ref 19-21). Here, the approach by Okajima et al. (Ref 21) is modified by altering the position of an artificially introduced defect to within the coating structure. This modified approach offers measurement of the in-plane toughness within the coating thickness as opposed to the interfacial toughness as measured by the previous method.

For this evaluation, deposition was halted at one-half the targeted total thickness and a defect was introduced in the form of a 3.2 mm graphite ring (∼ 10-25 μm thickness) around the edge of the coating face. After the ring was

applied, deposition was continued to the desired final thickness here, 350 μm. The graphite ring acts within the structure to limit bonding and create a defect resembling a crack. Following full deposition and standard adhesion test preparation, samples were pulled according to ASTM C633 standards, which are described in more detail in the following sections. Supporting equations for analysis of the load at failure and toughness derivation are shown below. In the following equations, μ_1 and μ_2 represent the shear moduli (calculated from Eq 13), while v_1 and v_2 represent the Poisson's ratio of the substrate (0.33) and coating (0.2), respectively, based on literature values (Ref 21). These are

used to calculate the constants, k, k_1, and k_2, which are in turn used to calculate Dundur's parameter, α. The geometric factor, $G(c/R)$, is a function of the width of the carbon ring, c, and the radius of the substrate, R. Equation 12 relates these factors with the critical load, P_c, yielding a final value for fracture toughness (Ref 21).

$$k = \mu_1/\mu_2 \tag{Eq 7}$$

$$k_1 = (3 - 4v_1) \tag{Eq 8}$$

$$k_2 = (3 - 4v_2) \tag{Eq 9}$$

$$\alpha = \frac{k(k_1 + 1) - (k_2 + 1)}{k(k_1 + 1) + (k_2 + 1)} \tag{Eq 10}$$

$$G\left(\frac{c}{R}\right) = \frac{1}{2}\left[1 + \frac{1}{2}\left(\frac{c}{R}\right) + \frac{3}{8}\left(\frac{c}{R}\right)^2 - 0.363\left(\frac{c}{R}\right)^3 + 0.731\left(\frac{c}{R}\right)^4\right] \tag{Eq 11}$$

$$K_{Ic} = (1 - \alpha)^{1/2}\frac{P_c}{\pi c^2}\sqrt{\pi c\left(1 - \frac{c}{R}\right)} \cdot G\left(\frac{c}{R}\right) \tag{Eq 12}$$

$$\mu = \frac{E}{2(1 + v)} \tag{Eq 13}$$

Tensile Elongation Method for Fracture Testing

Tensile testing of TS coatings has been used for measurement of coating strength contribution, strain to fracture, and other coating and substrate properties (Ref 22-24). Failure in the coating system typically occurs in the form of horizontal band cracking, normal to the tensile direction. This is similar to cracking patterns seen in PVD structures under tensile loading, as described by Ganne et al. (Ref 25). In that work, fracture toughness was calculated from the strain at fracture of the coating and the elastic modulus properties of both the coating and substrate, based on the previous assessments of brittle films by Hu and Evans (Ref 26). In the adaptation here, the same tensile approach is used. Coatings were deposited on both sides of steel tensile bars, covering the gauge length of the bar. Loading was applied to both ends of the substrate, with shear forces acting upon the coating during elongation. The full methodology is described in Ref 22-24. Crack detection was determined by analysis of images recorded during testing, which was then related to a critical stress and strain at which failure was first observed in the coatings.

One advantage of this method is the incorporation of the coating residual stress, which was calculated here from beam curvature methods. Full descriptions of the beam curvature measurements can be found elsewhere (Ref 27-29). This inclusion is important as the implications of residual stress, will be shown later to produce measurement complications, especially in the HVOF coatings.

Equation 14 and 15 detail the fracture energy in this system. In these equations, $\sigma_{xx,c}$, $\varepsilon_{xx,c}$, τ_y, and E' represent the critical stress, critical strain, substrate shear stress, and plane-strain elastic modulus, respectively (Ref 25). Superscripts f and s indicate the variable in question refers to the coating (film) or substrate. Thickness is denoted by t, and F is a function of elastic moduli contrast between the substrate and coating. In Eq 14, $\sigma_{xx,c}$ is calculated from the elastic modulus of the film and $\varepsilon_{xx,c}$, which was determined by image acquisition during testing. In Eq 15, τ_y (118 MPa) was calculated from the substrate yield strength (205 MPa) and the value of F (0.71) was interpolated based on values used by Hu and Evans (Ref 26).

$$\sigma_{xx,c}^f \approx E^f \varepsilon_{xx,c}^s \tag{Eq 14}$$

$$K_{Ic} = \left[E'\left(\frac{\left(\sigma_{xx,c}^f\right)^2 t^f}{E^f}\left[\pi F\left(\frac{E^s}{E^f}\right) + \frac{\sigma_{xx,c}^f}{3*\tau_y^s}\right]\right)\right]^{1/2} \tag{Eq 15}$$

Microscopy

Metallographic cross sections were prepared by sectioning samples using a high-speed diamond saw followed by standard metallographic epoxy infiltration. Samples were polished to a sub-micron finish (EcoMet 3, Buehler Inc., Lake Bluff, IL, USA). Backscattered scanning electron microscope (BSE-SEM) (Hitachi TM3000, Japan) was used to observe coating cross sections and crack propagation resulting from the different testing methods. Additional observation of notch dimensions and surface features was performed with an optical microscope (Nikon, Epiphot 200, Brighton, MI). Porosity values were determined from an average of 10 images using a thresholding technique.

Hardness

One kilogram Knoop hardness indentations were made on the polished cross sections of each sample. Ten to twenty indents were performed on each sample, with an average approximate spacing between indents equivalent to five indents, and the final given hardness value taken from an average of these measurements.

Adhesion

Adhesion was measured by standard ASTM C633, using a commercial adhesive (EP15ND-2, Masterbond, Hackensack, NJ) to join the coating on the 25.4 mm adhesion button to the encounter mating surface of the other button. Joined buttons were cured for 1 h at 150 °C. After curing, a
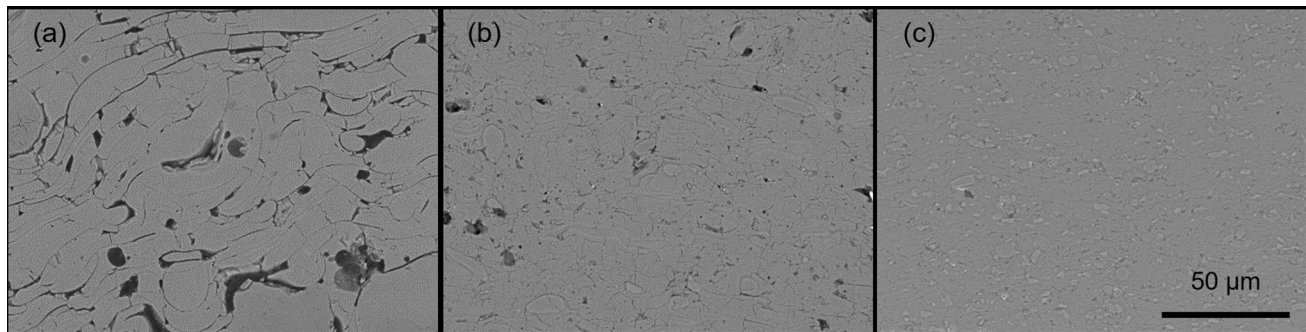
Fig. 4 Scanning electron microscope images of the Al_2O_3 coating cross sections show highly porous and lamellar features in the rod flame spray coating (a), dense, highly defected features with microcracking in the APS coating (b), and highly dense and lamellar features within the HVOF coating (c)

uniaxial tensile machine (Instron, Norwood, MA) was used to load the sample at 1 mm/min constant displacement, until separation occurred. This maximum load was then used for calculation of adhesion strength.

Indentation Modulus

Modulus measurements were calculated based on a standard Oliver–Pharr method, using multiple instrumented indentations on the coating surface (Ref 30). Indentation was performed using a 1.5 mm spherical indenter applied to a 5 N maximum load, with a minimum of 20 indents on each sample and 100 μm spacing between indents. The average response of the applied load was extracted into a single reported modulus value.

Results

Microstructure Evaluation

SEM evaluation reveals a range of microstructures for the different Al_2O_3 coatings produced by the three different processes. These range from lamellar and highly porous in the flame spray coating to a near-full density structure in the HVOF coating, shown in Fig. 4. These structures have been evaluated in other works (Ref 23, 31) and demonstrate the potential variety of structures that can be achieved via TS deposition techniques. This variation in structure has significant influence on standard mechanical property parameters, which are reported in Table 3.

Indentation modulus, flexural modulus, and Knoop hardness relate inversely to porosity, exponentially in the case of the hardness. Indentation modulus values are higher than their flexural counterparts, as they represent a localized measurement of stiffness, under compression. This differs from flexural modulus measurements, which incorporate effects from the overall porosity and potential

splat sliding in-plane, effectively decreasing the overall stiffness. Adhesion strength trends higher with decreasing porosity in the case of the flame spray and APS coatings, however, drops significantly for the HVOF coating. This is likely due to the large residual stresses of the HVOF coatings stemming from CTE mismatch exaggerated by the high substrate temperatures during deposition, which act upon the coating/substrate interface. The residual stresses (all compressive) and peak substrate temperatures for all three coatings are listed in Table 4.

Three-Point Bending: Benchmarking with Standard Materials

Three-point bending was performed on a range of standard materials, namely bulk Al_2O_3, sintered silicon carbide (s-SiC), and fused quartz glass (f-Quartz). Results for each of these values, with both SENB and chevron techniques reveal a close correlation to a range of literature measurements, validating the setup and methodology used for evaluation of the TS materials presented in Fig. 5.

Three-Point Bending: Parametric Variation of APS Al_2O_3

The results of the bend test parametric study are shown in Fig. 6(a) for thin (1.63 mm) samples and Fig. 6(b) for thick (3.25 mm) samples. Variations in notch sharpness, depth, and sample thickness were introduced to the APS samples to examine how they affect the calculated fracture toughness. The clearest and most expected trend was the increase in toughness of the sintered samples compared to the as-sprayed samples. This is a well-documented response in thermal spray ceramics and represents an articulated change in the fracture behavior of the material (Ref 9, 10, 42, 43).

The behavior stemming from the rest of the variable changes is also dependent on this difference between as-

Table 3 Measurement results of the three as-sprayed Al_2O_3 coating variants

Deposition torch/process designation	Porosity, %	Indentation modulus, GPa	Flexural modulus, GPa	Knoop hardness, HK, 1 kg	Adhesion strength, MPa	Shear modulus, μ, GPa
Rod flame spray	16.2 ± 3.0	22 ± 10	8.7 ± 0.8	37 ± 8	20 ± 1	9.2 ± 4.2
APS	7.7 ± 2.0	66 ± 12	32.0 ± 1.6	364 ± 63	40 ± 12	27.5 ± 5.0
HVOF	2.2 ± 1.0	171 ± 30	122.9 ± 3.9	1240 ± 154	9 ± 3	71.3 ± 12.5

Table 4 Peak temperature and residual stress measurements of the three Al_2O_3 coating variants

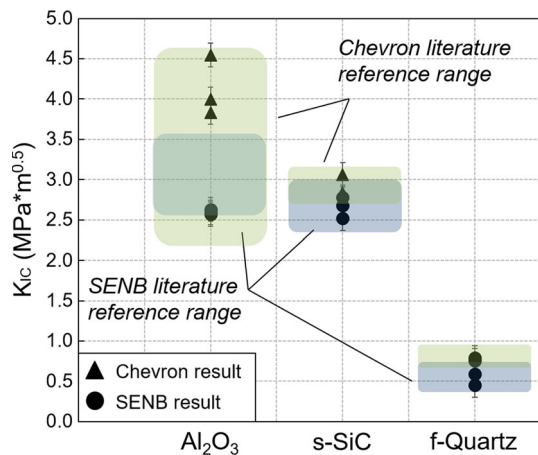| Deposition torch/process designation	Rod flame spray	APS	HVOF
Residual stress, MPa	− 60 ± 10	− 165 ± 18	− 379 ± 46
Peak substrate temperature, °C	245 ± 6	346 ± 60	716 ± 47

Fig. 5 Three-point bend testing results of standard bulk materials, including Al_2O_3, sintered SiC, and fused quartz, in both SENB and chevron notch geometries, with reference value ranges for each material and method shown in the shaded background (Ref 32-42)

sprayed and sintered samples. The as-sprayed samples showed slight, but significant differences between the standard and razor enhanced notches, with toughness values slightly lower with the razor enhanced notch. However, the difference in toughness stemming from notch sharpness in the sintered samples fell within the standard deviation of the measurements.

This change in behavior between the as-sprayed and sintered samples is also seen with respect to the change in the notch-to-depth ratio, a/W, as is highlighted with the overlays in Fig. 6. As the ratio increases, there is a strong increase in the measured toughness of the sintered samples. In the as-sprayed samples, this trend is neutral relative to the standard deviation. Both behaviors are likely related to the increase in density, structure, and stiffness resultant from the sintering process. This changes how stress is concentrated at the notch tip and has implications with regard to how the available energy in the system will drive

propagation or be diffused. Further explanation will be elaborated on in the discussion section.

Additional observations can be made based on overall sample thickness and general notch geometry. In Fig. 7(a), a comparison of the three different thickness levels is shown. There is a limited difference between the 1 and 1.63 mm samples, but a significant increase in toughness of nearly 48% to 2.4 ± 0.1 MPa$\sqrt{}$m for the 3.25 mm sample. The 3.25 mm samples are used to compare the measured difference between the chevron and SENB notches as there is a requisite minimum thickness to successfully cut the chevrons. There is no difference between the two notch geometries in the flame spray samples; however, there is a slight increase seen with the denser APS structure with the SENB notch, as compared to the chevron notch. HVOF samples were not tested due to limitations in the thickness to which they could be successfully deposited.

Non-bend Test Evaluation

All three coating variants were assessed with both the modified adhesion method and the tensile elongation method. Although promising for this limited set of materials, toughness measurements from the modified adhesion method and tensile elongation will be referred to as *apparent* fracture toughness to assert that there is still development work ongoing. Results from the modified tensile adhesion results are shown in Fig. 8(a), with the APS Al_2O_3 showing the highest toughness value of 1.4 ± 0.4 MPa$\sqrt{}$m. Figure 8(b) shows the final failure images from the three coatings. The introduced graphite ring can be seen on the edges of the samples, where the fracture originated. In the flame spray samples, "bleeding" of the excess applied graphite can be seen having spread in low amounts toward the center of the sample; however, this does not appear to have a deleterious effect on the measurement. This behavior does give some insight into the lamellar nature and resulting horizontal transport of the
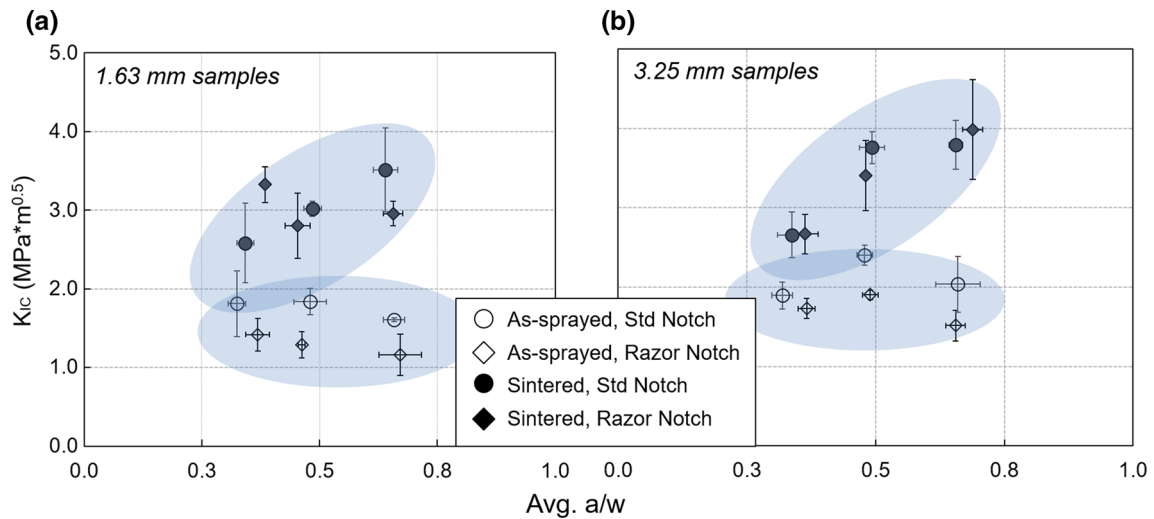
Fig. 6 SENB results at medium (a) and high (b) thickness, with variation in notch-to-depth (a/W) ratio, heat treatment state, and root radius. Highlighted are trends between the notch-to-depth ratio and the heat treatment state
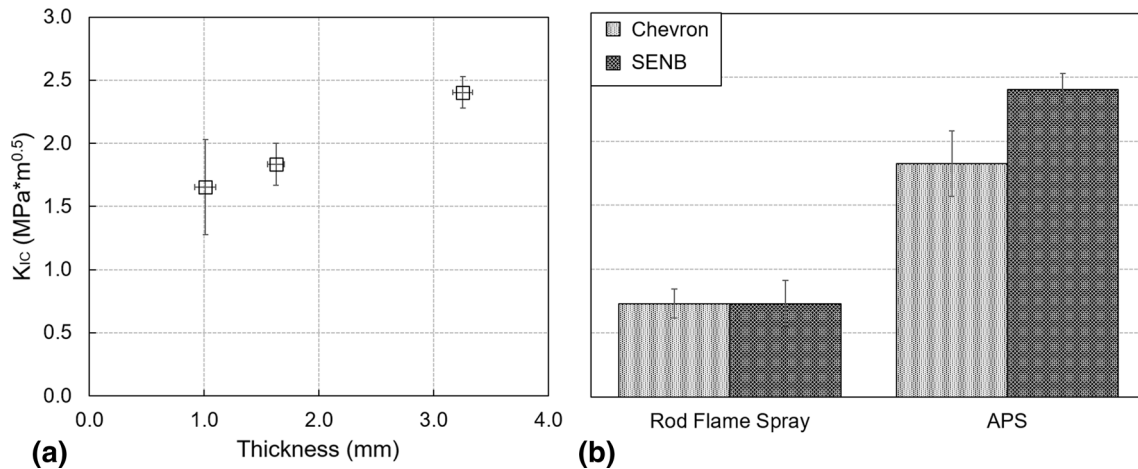

Fig. 7 Comparison of the SENB toughness results as a function of sample thickness (a) and comparison of chevron and standard SENB toughness results using the 3.25 mm samples (b)

graphite film in the flame spray coating. There was minimal spreading of the applied graphite layer in the APS case. HVOF samples showed a failure that was much less defined and partially occurs at the substrate interface, which is reflected in the high error bars in Fig. 8(a). This is likely due to the high interfacial stress that was previously mentioned in context of the ASTM C633 adhesion measurement.

Similar trends are seen in the apparent fracture toughness results for the tensile elongation method shown in Fig. 9(a), with the highest measured toughness for the APS case yielding a value of 2.1 ± 0.2 MPa$\sqrt{}$m. Surface images are shown in Fig. 9(b), which indicate large differences between the flame spray and HVOF coatings. The high density, elastic energy, and stiffness of the HVOF coatings

result in a much more brittle fracture evidenced by the many horizontal, angular bands and smaller segments. The flame spray coating shows a range of cracking behavior, encompassing multiple directions and is much more discontinuous. The APS coating lies in-between the two more extreme failure types.

Discussion

Parametric Variation with Heat Treatment

As mentioned previously, the difference in behavior of the as-sprayed to sintered samples in the parametric study is notable. This stems from the differences in material
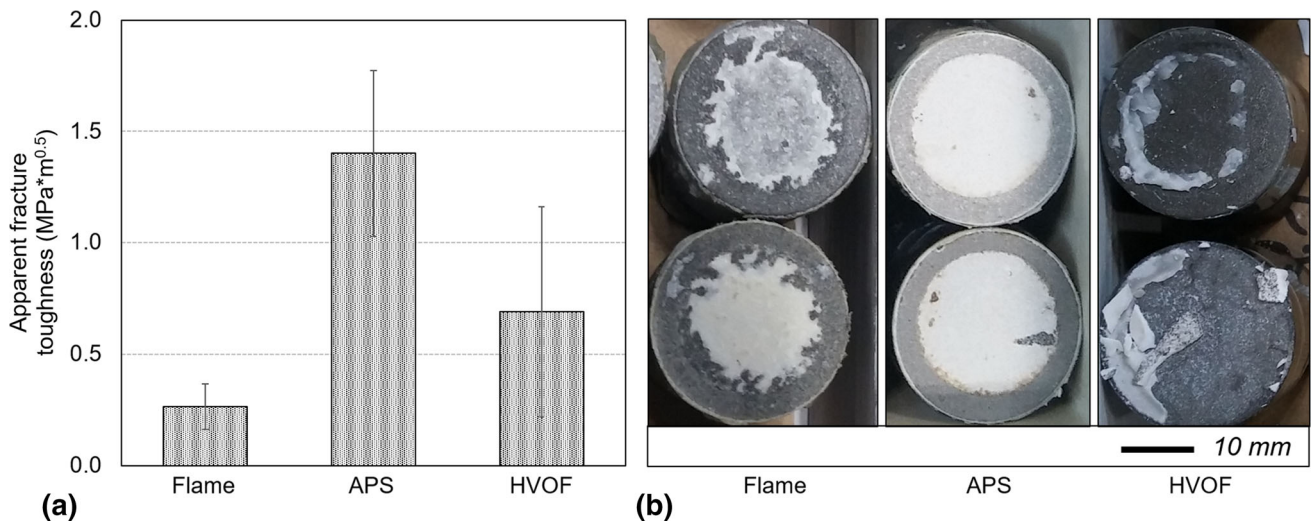
Fig. 8 Modified tensile adhesion calculated toughness results for the three coating variants (a) and the final fracture images (b) of the flame spray, APS, and HVOF Al_2O_3 materials
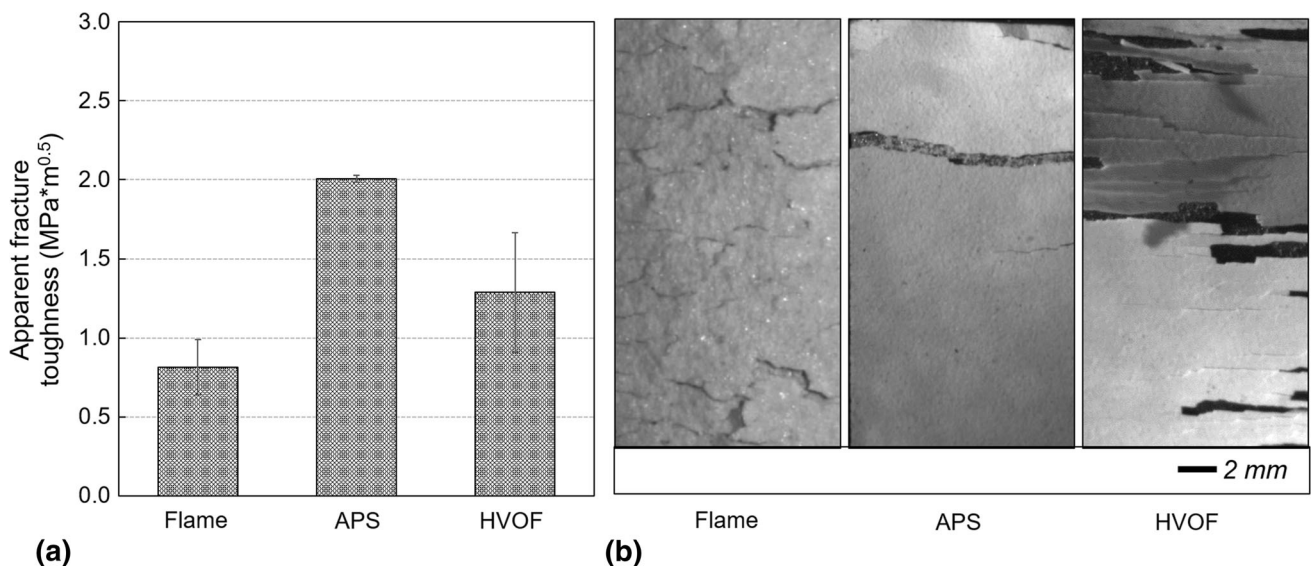

Fig. 9 Calculated fracture toughness values measured from the tensile elongation of the three different process coatings (a) and the final fracture images of the three coatings (b)

structure, density, and stiffness after the heat treatment, which has been well documented in the literature (Ref 10, 44-46). Even after a relatively short 24-h sinter at 1200 °C, there is evidence of crack healing, densification, and a reduction in sharp internal features. This change can result in differences in how stress is distributed over the encompassing structures. X-ray diffraction revealed changes to the phase structure after the heat treatment; however, the mechanical properties are more strongly determined by the changes to the microstructural features (Ref 9, 47). In the as-sprayed samples, the structure beneath the notch where there is a stress concentration has some limited ability to undergo localized relief and splat sliding (Ref 48-

50). However, after sintering this ability is reduced. This difference has implications in behavioral changes and response regarding the notch sharpness and notch-to-depth (a/W) ratio.

The sharpness of the notches can change the stress concentration, which ultimately drives crack propagation. In samples with the standard notch, the stress concentration can be slightly redistributed across a broader area below the crack tip. The razor enhanced notch acts to sharply concentrate the stress to a more finite point, where propagation would occur more readily and slightly lower the measured toughness. In the as-sprayed samples, there is a certain amount of compliance and nonlinearity under the

standard notch that enables stress redistribution within the structure. Alternatively, a sharp notch more readily localizes a stress concentration and results in a lower measured toughness. In the sintered samples with reduced compliance (flexural modulus increases by 74% to 55.5 ± 7.6 GPa), the stress concentration results in crack propagation that follows more expected linear-elastic behaviors. Over this small range, notch sharpness has a limited influence on the measured toughness (Ref 35).

Notch depth is specified in the ASTM standard to be 50 ± 5% of the sample thickness, so the variations here to a/W at the low and high ends are intentionally outside of the measurement specifications. However, this intentional variation can be used to gain some additional insight to the application of the method. In the as-sprayed samples, there is no substantial measured change in toughness as the a/W ratio is changed. In the sintered samples, the measured toughness increases with increasing a/W. This discrepancy may be due to the available compliance in the as-sprayed structure normalizing changes to the stress concentration. This appears counter to expectations of system behavior based on linear-elastic fracture mechanics.

Nonlinearity can be seen in TS coatings under low applied loads (either mechanical or thermal), cyclic loads, or near-steady state conditions. For example, Liu et al. (Ref 51) and Dwivedi et al. (Ref 52) show nonlinearity under these lower loads or loading rate conditions. While these conditions are not representative of the standard three-point bending here, small and localized nonlinear behaviors may appear in the as-sprayed, more compliant samples. Results in the context of changing conditions such as notch depth and with varying compliance structures require additional considerations. It has been demonstrated by Damani and Lutz (Ref 14) and Choi et al. (Ref 8) that TS samples can be approximated as linear-elastic within a single plane of fracture. This allows for use of methods that would otherwise not be strictly applicable to complex systems, such as TS coatings.

The response of notch depth parameter in affecting the calculated toughness can be simply modeled using the constituent equations (Eq 3 and 4), which can indicate the sensitivity to the input parameters. This is shown in Fig. 10, where the measured fracture toughness sharply increases after the a/W ratio trends above 0.5, deviating from the relatively linear behavior prior to that mark. At notch depths > 0.6, the magnitude of the potential error increases linearly with $F\left(\frac{a}{w}\right)$. The exponential rise in this modeled result indicates a potential significant effect of the notch depth term on the calculated toughness result (and as a function of the geometric factors that are described within the equation).
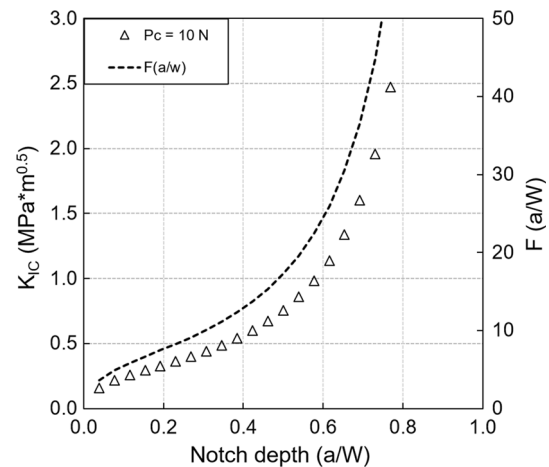

Fig. 10 Modeled response of the fracture toughness measurement and $F\left(\frac{a}{w}\right)$ plotted against notch depth

The parametric changes to a/W, notch sharpness, and thickness will alter the measurement response; however, it is important to mention that these changes can also be reflections of the measurement calculations operating outside of their intended boundary conditions. The calculated toughness result will reflect these changes; however, the intrinsic toughness of the material has not changed with variations in notch sharpness or depth.

HVOF Deposition of Ceramic Materials

Toughness measurement of the HVOF Al_2O_3 materials provided a number of challenges which seem to primarily originate from high residual stresses generated during deposition. HVOF processes, especially in the case of ceramic deposition, typically transfer a significant amount of thermal energy to the substrate. This is partially related to the high temperatures necessary to melt the ceramic material (here, Al_2O_3, with a melting point > 2000 °C) and the requisite high-volume flow of the HVOF combustion gases needed to achieve these temperatures. To contrast, the APS process allows for complete material melting with less mass flow. Even with considerable air cooling, the high enthalpy HVOF process results in high substrate temperatures (See Table 4). After coating deposition, the large temperature changes due to cooling, coupled with the large coefficient of thermal expansion mismatch between Al_2O_3 and low-carbon steel, results in considerable residual stresses. The residual stress has a strong influence on the coating adhesion, which can result in measurement uncertainty. This is captured by the error bars of the modified tensile method, and to a lesser extent the tensile elongation data. The interfacial residual stresses can cause delamination along the interface, which result in failure occurring at that location prior to cracking in the coating
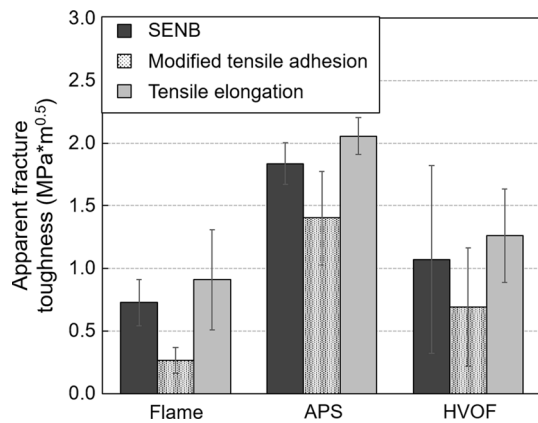
Fig. 11 Comparison of toughness values calculated by each method

itself. The residual stresses for each spray process are listed in Table 4.

Relating Toughness Measurements and Orientation Differences

Toughness measurements from three methodologies for each of the three coatings are directly compared in Fig. 11. There is strong agreement between the SENB and the tensile elongation measurement values; however, a lower value is found in the modified tensile adhesion method. This is due to the difference in testing orientations (out-of-plane versus in-plane toughness) and is explained in more detail below. This comparison indicates a successful utilization of different methodologies to measure toughness of these different structures.

Measurement orientation and coating anisotropy is of significant concern in TS coatings. SENB and tensile elongation both represent out-of-plane toughness measurements, while the modified tensile adhesion method gives in-plane results. The results here show a decrease of 25-65% for the in-plane fracture measurements, which has also been shown experimentally in prior TS material testing (Ref 9).

The relative decrease in the in-plane toughness varies for each of the coatings and is by far greatest for the flame spray sample. This exaggerated decrease for in-plane toughness can be attributed to the lamellar microstructural features and large splat sizes that emphasize coating anisotropy. The HVOF coating also tends to show a more lamellar structure, but the orientation effects may be masked by both its high density and strong internal cohesion (which is also seen in the APS structure). The higher densities and internal cohesion of the APS and HVOF coatings reduce the effects of coating anisotropy by creating a more homogenous structure and therefore reduce the relative decrease of the in-plane toughness result.

Conclusion

The goal of this work was to present a comprehensive assessment of toughness measurement in TS materials that can be utilized for future development. Often measurement methods or applications are not accurately applied in light of system specific constraints. This can lead to damaging assumptions about the material and technology. Recognizing the unique attributes of TS coatings is necessary when applying existing testing methods or adapting literature/industrial methods to TS materials.

SENB has been shown to enable well-substantiated toughness measurements, but it can be difficult to fabricate requisite free-standing samples and test correctly. The results of the parametric study demonstrate that a range of factors can drastically affect the measurement result, even within one material system. Due to this testing sensitivity, alternative methods can be useful in supplementing existing results and addressing material anisotropy.

There is good agreement among the toughness results from the additional supplementary measurement techniques, and they enable investigation into the effects of orientation-dependent results. In TS materials, the in-plane orientation is often of critical concern. For that case, results calculated using the modified adhesion method indicate a 25-65% lower in-plane versus out-of-plane toughness result, dependent on microstructure. However, as some of these methods are still undergoing development, caution is urged in their explicit application without considering a larger range of methods. But based on the results shown, these methods can be validated for specific usage and offer practical techniques to measure multi-orientation toughness.

References

1. J. Shackelford and R.H. Doremus, *Ceramic and Glass Materials: Structure, Properties and Processing*, Springer, 2008, p 1-202
2. M.F. Ashby, *Materials Selection in Mechanical Design*, Butterworth-Heinemann, Oxford, 2011
3. R.O. Ritchie, The Conflicts Between Strength and Toughness, *Nat. Mater.*, 2011, **10**, p 817
4. F. Bouville, E. Maire, S. Meille, B. Van de Moortèle, A.J. Stevenson, and S. Deville, Strong, Tough and Stiff Bioinspired Ceramics From Brittle Constituents, *Nat. Mater.*, 2014, **13**(5), p 508-514
5. F.W. Zok and C.G. Levi, Mechanical Properties of Porous-Matrix Ceramic Composites, *Adv. Eng. Mater.*, 2001, **3**(1-2), p 15-23

6. G.D. Quinn and R.C. Bradt, On the Vickers Indentation Fracture Toughness Test, *J. Am. Ceram. Soc.*, 2007, **90**(3), p 673-680

7. N.P. Padture, M. Gell, and E.H. Jordan, Thermal Barrier Coatings for Gas-Turbine Engine Applications, *Science*, 2002, **296**(5566), p 280-284

8. S.R. Choi, D. Zhu, and R.A. Miller, Fracture Behavior Under Mixed-Mode Loading of Ceramic Plasma-Sprayed Thermal Barrier Coatings at Ambient and Elevated Temperatures, *Eng. Fract. Mech.*, 2005, **72**(13), p 2144-2158

9. G.M. Smith, M. Resnick, B. Kjellman, J. Wigren, G. Dwivedi, and S. Sampath, Orientation-Dependent Mechanical and Thermal Properties of Plasma-Sprayed Ceramics, *J. Am. Ceram. Soc.*, 2018, **101**(6), p 2471-2481

10. G. Dwivedi, V. Viswanathan, S. Sampath, A. Shyam, and E. Lara-Curzio, Fracture Toughness of Plasma-Sprayed Thermal Barrier Ceramics: Influence of Processing, Microstructure, and Thermal Aging, *J. Am. Ceram. Soc.*, 2014, **97**(9), p 2736-2744

11. E.M. Donohue, N.R. Philips, M.R. Begley, and C.G. Levi, Thermal Barrier Coating Toughness: Measurement and Identification of a Bridging Mechanism Enabled by Segmented Microstructure, *Mater. Sci. Eng. A*, 2013, **564**, p 324-330

12. G. Dwivedi, K. Flynn, M. Resnick, S. Sampath, and A. Gouldstone, Bioinspired Hybrid Materials from Spray-Formed Ceramic Templates, *Adv. Mater.*, 2015, **27**(19), p 3073-3078

13. G.D. Quinn and J.J. Swab, Fracture Toughness of Glasses as Measured by the SCF and SEPB Methods, *J. Eur. Ceram. Soc.*, 2017, **37**(14), p 4243-4257

14. R.J. Damani and E.H. Lutz, Microstructure, Strength and Fracture Characteristics of a Free-Standing Plasma-Sprayed Alumina, *J. Eur. Ceram. Soc.*, 1997, **17**(11), p 1351-1359

15. *Standard Test Method for Measurement of Fracture Toughness*, E 1820, ASTM International 2017

16. *Standard Test Methods for Determination of Fracture Toughness of Advanced Ceramics at Ambient Temperature*, C 1421, ASTM International 2018

17. *Standard Test Method for Adhesion or Cohesion Strength of Thermal Spray Coatings*, C 633, ASTM International 2013

18. X. Luo, G.M. Smith, and S. Sampath, On the Interplay Between Adhesion Strength and Tensile Properties of Thermal Spray Coated Laminates—Part I: High Velocity Thermal Spray Coatings, *J. Therm. Spray Technol.*, 2018, **27**(3), p 296-307

19. G. Qian, T. Nakamura, C.C. Berndt, and S.H. Leigh, Tensile Toughness Test and High Temperature Fracture Analysis of Thermal Barrier Coatings, *Acta Mater.*, 1997, **45**(4), p 1767-1784

20. M. Watanabe, S. Kuroda, K. Yokoyama, T. Inoue, and Y. Gotoh, Modified Tensile Adhesion Test for Evaluation of Interfacial Toughness of HVOF Sprayed Coatings, *Surf. Coat. Technol.*, 2008, **202**(9), p 1746-1752

21. Y. Okajima, T. Nakamura, and S. Sampath, Effect of Powder Injection on the Interfacial Fracture Toughness of Plasma-Sprayed Zirconia, *J. Therm. Spray Technol.*, 2013, **22**(2), p 166-174

22. A. Vackel, T. Nakamura, and S. Sampath, Mechanical Behavior of Spray-Coated Metallic Laminates, *J. Therm. Spray Technol.*, 2016, **25**(5), p 1009-1019

23. G.M. Smith, O. Higgins, and S. Sampath, In-situ Observation of Strain and Cracking in Coated Laminates by Digital Image Correlation, *Surf. Coat. Technol.*, 2017, **328**, p 211-218

24. G.M. Smith and S. Sampath, Sustainability of Metal Structures via Spray-Clad Remanufacturing, *JOM*, 2018, **70**(4), p 512-520

25. T. Ganne, J. Crépin, S. Serror, and A. Zaoui, Cracking Behaviour of PVD Tungsten Coatings Deposited on Steel Substrates: The Influence of Film Thickness, *Acta Mater.*, 2002, **50**, p 4149-4163

26. M.S. Hu and A.G. Evans, The Cracking and Decohesion of Thin Films on Ductile Substrates, *Acta Mater.*, 1989, **37**(3), p 917-925

27. S. Kuroda, Y. Tashiro, H. Yumoto, S. Taira, H. Fukanuma, and S. Tobe, Peening Action and Residual Stresses in High-Velocity Oxygen Fuel Thermal Spraying of 316L Stainless Steel, *J. Therm. Spray Technol.*, 2001, **10**(2), p 367-374

28. J. Matejicek and S. Sampath, In Situ Measurement of Residual Stresses and Elastic Moduli in Thermal Sprayed Coatings: Part 1: Apparatus and Analysis, *Acta Mater.*, 2003, **51**(3), p 863-872

29. A. Valarezo and S. Sampath, An Integrated Assessment of Process-Microstructure-Property Relationships for Thermal-Sprayed NiCr Coatings, *J. Therm. Spray Technol.*, 2011, **20**(6), p 1244-1258

30. W.C. Oliver and G.M. Pharr, An Improved Technique for Determining Hardness and Elastic Modulus Using Load and Displacement Sensing Indentation Experiments, *J. Mater. Res.*, 1992, **7**(6), p 1564-1583

31. G.M. Smith, M. Resnick, K. Flynn, G. Dwivedi, and S. Sampath, Nature Inspired, Multi-Functional, Damage Tolerant Thermal Spray Coatings, *Surf. Coat. Technol.*, 2016, **297**, p 43-50

32. J. Kubler, Fracture Toughness of Ceramics Using the Sevnb Method: Preliminary Results, *Proceedings of the 21st Annual Conference on Composites, Advanced Ceramics, Materials, and Structures—B: Ceramic Engineering and Science*, ed., J.P. Singh, 1997

33. L. Vargas-Gonzalez, R.F. Speyer, and J. Campbell, Flexural Strength, Fracture Toughness, and Hardness of Silicon Carbide and Boron Carbide Armor Ceramics, *Int. J. Appl. Ceram. Technol.*, 2010, **7**(5), p 643-651

34. G.A. Gogotsi, Fracture Toughness of Ceramics and Ceramic Composites, *Ceram. Int.*, 2003, **29**(7), p 777-784

35. R. Damani, R. Gstrein, and R. Danzer, Critical Notch-Root Radius Effect in SENB-S Fracture Toughness Testing, *J. Eur. Ceram. Soc.*, 1996, **16**(7), p 695-702

36. R.G. Munro, Material Properties of a Sintered α-SiC, *J. Phys. Chem. Ref. Data*, 1997, **26**(5), p 1195-1203

37. M.G. Mueller, V. Pejchal, G. Žagar, A. Singh, M. Cantoni, and A. Mortensen, Fracture Toughness Testing of Nanocrystalline Alumina and Fused Quartz using Chevron-Notched Microbeams, *Acta Mater.*, 2015, **86**, p 385-395

38. R.E. Grimes, G.P. Kelkar, L. Guazzone, and K.W. White, Elevated-Temperature R-Curve Behavior of a Polycrystalline Alumina, *J. Am. Ceram. Soc.*, 1990, **73**(5), p 1399-1404

39. R.F. Krause, Rising Fracture Toughness from the Bending Strength of Indented Alumina Beams, *J. Am. Ceram. Soc.*, 1988, **71**(5), p 338-343

40. P. Auerkari, Mechanical and Physical Properties of Engineering Alumina Ceramics, Technical Research Centre of Finland, *VTT Tiedotteita - Meddelanden - Res. Notes*, 1996, **1792**, p 1–26

41. G. Žagar, V. Pejchal, M.G. Mueller, L. Michelet, and A. Mortensen, Fracture Toughness Measurement in Fused Quartz Using Triangular Chevron-Notched Micro-cantilevers, *Scr. Mater.*, 2016, **112**, p 132-135

42. S.M. Wiederhorn, Fracture Surface Energy of Glass, *J. Am. Ceram. Soc.*, 1969, **52**(2), p 99-105

43. Y. Tan, J.P. Longtin, S. Sampath, and H. Wang, Effect of the Starting Microstructure on the Thermal Properties of As-Sprayed and Thermally Exposed Plasma-Sprayed YSZ Coatings, *J. Am. Ceram. Soc.*, 2009, **92**(3), p 710-716

44. W. Chi, S. Sampath, and H. Wang, Ambient and High-Temperature Thermal Conductivity of Thermal Sprayed Coatings, *J. Therm. Spray Technol.*, 2006, **15**(4), p 773-778

45. W. Chi, S. Sampath, and H. Wang, Microstructure-Thermal Conductivity Relationships for Plasma-Sprayed Yttria-Stabilized Zirconia Coatings, *J. Therm. Spray Technol.*, 2008, **91**(8), p 2636-2645

46. Z. Wang, A. Kulkarni, S. Deshpande, T. Nakamura, and H. Herman, Effects of Pores and Interfaces on Effective Properties of Plasma Sprayed Zirconia Coatings, *Acta Mater.*, 2003, **51**(18), p 5319-5334

47. E. García, M.I. Osendi, and P. Miranzo, Thermal Diffusivity of Porous Cordierite Ceramic Burners, *J. Appl. Phys.*, 2002, **92**(5), p 2346-2349

48. R. Musalek, J. Matejicek, M. Vilemova, and O. Kovarik, Non-linear Mechanical Behavior of Plasma Sprayed Alumina Under Mechanical and Thermal Loading, *J. Therm. Spray Technol.*, 2010, **19**(1-2), p 422-428

49. R. Mušálek, O. Kovářík, and J. Matějíček, In-situ Observation of Crack Propagation in Thermally Sprayed Coatings, *Surf. Coat. Technol.*, 2010, **205**(7), p 1807-1811

50. D. Zhu and R.A. Miller, Sintering and Creep Behavior of Plasma-Sprayed Zirconia- and Hafnia-Based Thermal Barrier Coatings, *Surf. Coat. Technol.*, 1998, **108-109**, p 114-120

51. Y. Liu, T. Nakamura, G. Dwivedi, A. Valarezo, and S. Sampath, Anelastic Behavior of Plasma-Sprayed Zirconia Coatings, *J. Am. Ceram. Soc.*, 2008, **91**(12), p 4036-4043

52. G. Dwivedi, T. Nakamura, and S. Sampath, Controlled Introduction of Anelasticity in Plasma-Sprayed Ceramics, *J. Am. Ceram. Soc.*, 2011, **94**(s1), p s104-s111